CrossMark

ORIGINAL PAPER

In Situ Oxide Growth Characterization of Mn-Containing Ni–25Cr (wt%) Model Alloys at 1050 °C

T. Perez[1] · L. Latu-Romain[2] · R. Podor[3] · J. Lautru[3] ·
Y. Parsa[2] · S. Mathieu[1] · M. Vilasi[1] · Y. Wouters[2]

Abstract The oxidation behaviour of four model alloys with the composition Ni–25Cr–xMn (with $x = 0$, 0.5, 1 and 1.5 wt%) was investigated at 1050 °C in air by thermogravimetry and by in situ observations in an environmental scanning electron microscope (ESEM). The addition of manganese modifies the oxidation rate of Ni–25Cr alloys by (1) increasing the parabolic constant k_p compared to that for Ni–25Cr and (2) lowering the short-time oxidation rate. Regardless of the Mn concentration, in situ ESEM observations indicated the formation of spinel crystallites from the very beginning of the oxidation process. The size of the spinel crystallites was directly linked to the initial Mn concentration. The obtained results suggested that the formation of the spinel layer at the top of the chromia oxide scale rather than at the metal–oxide interface as thermodynamically expected must be attributed to the higher diffusion rate of Mn than Cr both in the lattice and at the grain boundary.

Keywords Nickel-based alloys · Manganese · High-temperature oxidation · Selective oxidation · Diffusion

Introduction

Most Ni–Cr industrial alloys dedicated to high-temperature applications contain minor alloying additions. These can be added to enhance a wide variety of alloy properties. Additions of Mn, Si, Al and Y are known to greatly modify the oxidation

✉ S. Mathieu
  stephane.mathieu@univ-lorraine.fr

[1] CNRS, IJL, University of Lorraine, 54500 Vandoeuvre lès Nancy, France

[2] CNRS, SIMaP, University of Grenoble Alpes, 38000 Grenoble, France

[3] Institut de Chimie Séparative de Marcoule, 30207 Bagnols sur Cèze Cedex, France

resistance. Briefly, the addition of aluminium allows the formation of an alumina subscale decreasing the overall oxidation rate [1, 2]; the addition of yttrium reduces the oxide growth kinetics and improves the adhesion and spallation resistance of both chromium and aluminium oxide scales [3–6]; manganese readily forms a spinel with chromium at the surface of the alloys in the first period of oxidation [3, 7, 8] and may affect the oxidation rate of Ni–Cr alloys [9]. Zurek et al. [9] noted a beneficial effect of Mn addition on the oxidation rate in the atmosphere containing a low amount of O_2 (Ar-4% H_2-7% H_2O), whereas Mn addition contributes to increase the alloy oxidation rate at high O_2 partial pressure [9, 10] and the spallation of the oxide scales [9].

Focusing the present study on the effect of manganese, it should be noted that the Gibbs energy associated with the oxidation of Mn in MnO is lower than that for the oxidation of Cr to Cr_2O_3. However, manganese oxide MnO is not favoured for the concentrations generally used (lower than 1 wt%) and generally, Mn contributes to the formation of an outer $MnCr_2O_4$ [1, 9–14] spinel layer at the top of a Cr_2O_3 layer. Based on the photoelectrochemistry results, Ledoux et al. [3] proposed that this top layer could be responsible for the change of the major point defects at the source of the Cr_2O_3 underlayer growth. Moreover, as this spinel layer forms at the oxide/air interface, it has been suggested [15] that it contributes to the decrease of chromia oxidation into volatile CrO_3 because of the lower chromium activity in $MnCr_2O_4$ than Cr_2O_3. In water vapour, the formation of $CrO_2(OH)_2$ is expected according to (1):

$$\frac{3}{2}O_2 + Cr_2O_3 + 2H_2O = 2CrO_2(OH)_2. \tag{1}$$
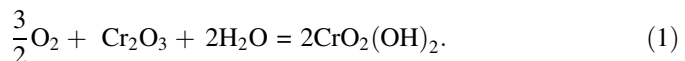
The partial pressure of $CrO_2(OH)_2$ has been reported to be significant at temperature starting from 750 °C [16]. This Mn effect may be crucial for industrial applications, for example, in fuel cells dealing with the water vapour containing environments. Consequently, a fundamental understanding of the Mn effect is important for the design of oxide scales with enhanced durability.

The present study focuses on the high-temperature oxidation of Ni–25Cr model alloys, with manganese additions in the range 0–1.5 wt%, in air. The present paper is a contribution to this study and mainly concentrates on the formation of these oxides forming at the top of these alloys. These were evaluated using in situ environmental SEM observations. Oxidation rates were also determined both by thermogravimetry and by furnace exposure for 100 h at 1050 °C in synthetic air (80% N_2 and 20% O_2).

Experimental Procedures

Materials

The alloys were prepared by high-frequency melting according to the starting composition given above. In this paper, all compositions are given in weight per

cent. Bulk elements with purities higher than 99.95% were placed into a water-cooled copper crucible and then enclosed in a silica tube. Prior to each experiment, three to four sequences of vacuuming and argon filling were performed in order to clean the atmosphere of the reactor. To avoid significant vapourization of the metallic elements, the melting was conducted under argon with the pressure of 0.8 atm. The samples were re-melted three times to ensure composition homogeneity and element distribution. Finally, the samples were gravity casted in a cold copper mould to obtain ingots with the diameter of 10 mm. The ingots were cut into 2-mm-thick slices using a diamond saw. The slices were then enclosed in a silica tube under argon to be heat-treated for 12 h at 1000 °C.

Oxidation Tests

Isothermal oxidation tests were conducted at 1050 °C using a symmetrical Setaram Setsys Evolution Device. Prior to each experiment, alloy samples with the diameter of 10 mm and thickness of 2 mm were ground with SiC paper up to 1200 grit. An alumina sample ($10 \times 10 \times 2$ mm) was previously tested as the control sample. The samples were hung in the hot zones of the furnaces by platinum wires. Industrial dry air was introduced into the reaction chamber at the flow rate of 1.5 L h^{-1}. Each sample was heated at 20 K min^{-1} up to the test temperature. Then, the experiments were performed for over 100 h at 1050 °C. The origin of each thermogram was taken to be the point at which the test temperature was reached because no significant weight increase was noted before reaching the isothermal dwell.

Sample Characterization

The in situ SEM oxidation experiments were performed in an environmental scanning electron microscope (FEI Quanta 200 FEG ESEM) equipped with a 1400 °C hot stage under an atmosphere of pure O_2 at 200 Pa. The samples were heated to the experimental temperature of 1050 °C under 200 Pa O_2 atmosphere at the rate of 50 K min^{-1}. The furnace is equipped with a specific thermocouple that allows a precise measure of the sample temperature [17]. When the target temperature is reached, the samples are heated isothermally for 1 h and images are continuously recorded at six different magnifications (250, 500, 1000, 2500, 5000 and 10,000 times) in order to record the information at different length scales. Frame times were adjusted according to the speed of the oxidation reaction. The frame times were typically 5 s during the first 10 min and 30 s during the last 15 min of the experiment. Image post-processing was performed using the Fiji ImageJ software [18]. First, the images were aligned. Then, the edges of the grains were drawn manually on 10–15 representative images for each alloy and the grain sizes were determined through the automatic "analyse particles" function of Fiji software.

Prior to observation, the cross sections were polished using wet 1200-grade and 4000-grade SiC paper and then a tightly woven cloth with 0.1-μm diamond paste. The composition was assessed by wavelength-dispersive spectrometry (WDS) using

a Cameca SX100 microprobe operated at 15 kV and 20 nA. Pure Ni, Mn and Cr were employed as standards for quantitative analysis. Under these analytical conditions, the spatial resolution was approximately 1–1.5 μm^3 for this kind of alloy and the uncertainty of measurement with the analysis conditions used was 0.07 wt%.

EDX maps at high resolution have been obtained to characterize the oxide scale. For this purpose, a transversal cross-sectional thin lamella was prepared using a dual focused ion beam scanning electron microscope (FIB-SEM, Zeiss Cross Beam NVision 40). STEM observations coupled to EDX investigations have been conducted on a transmission electron microscope at 200 keV (FEG-TEM, Jeol 2100F). EDX maps have been recorded with the spot size of 1 nm.

Results

Initial Alloys Microstructures

The actual composition (measured by electron probe micro-analysis) and the microstructure of the manufactured alloys after casting and heat treatment are shown in Table 1 and Fig. 1, respectively. The model alloy microstructures are very similar to each other. The grain size is between 70 and 200 μm (Table 1) except for the Ni–25Cr–0.5Mn sample which shows larger grains. The results of the microprobe analysis are in excellent agreement with the expected compositions.

Thermogravimetric Results

Figure 2a shows the mass change versus time evolution of the three samples during 100 h of isothermal oxidation at 1050 °C in air. The oxidation rate decreases with time for all alloys, but the shapes of the curves are slightly different. Spallation was observed during cooling for all considered alloys, but this phenomenon was more pronounced for Mn-containing alloys. The mass loss due to spallation can be easily observed (Fig. 2a) during cooling (the arrows in Fig. 2a point at the mass after cooling). It was found that the Ni–25Cr alloy had the smallest mass loss on cooling.

To better analyse the thermogravimetric results and assuming that the oxidation rate is inversely proportional to the mass of the oxide, the instantaneous k_p values deduced from (2) were determined and reported versus the oxidation time (Fig. 2b).

Table 1 Actual composition and grain size of the studied model alloys (determined by microprobe analysis)

Alloys (wt%)	Mn	Cr	Ni	Grain size (μm)
Ni–25Cr	0	25.6	72.5	110 ± 40
Ni–25Cr–0.5Mn	0.6	25.1	72.1	123 ± 95
Ni–25Cr–1Mn	1.1	25.5	70.9	151 ± 56
Ni–25Cr–1.5Mn	1.7	25.6	71.3	140 ± 49
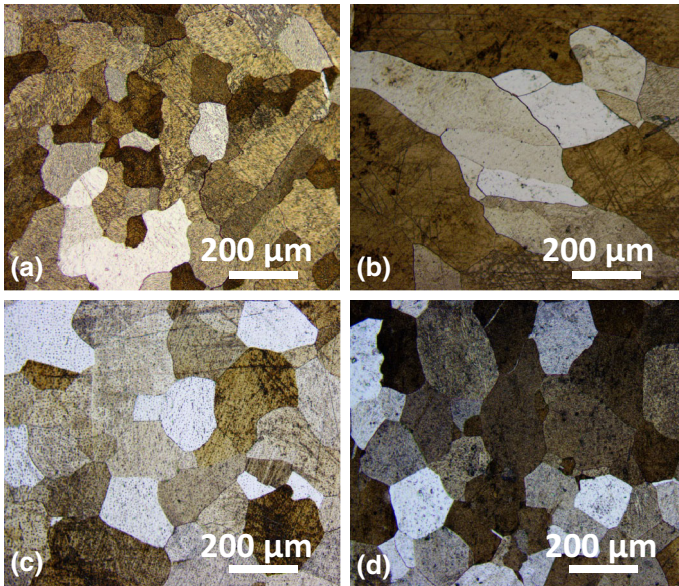
Fig. 1 Microstructure of the studied model alloys after heat treatment. **a** Ni–25Cr; **b** Ni–25Cr–0.5Mn; **c** Ni–25Cr–1Mn; **d** Ni–25Cr–1.5Mn
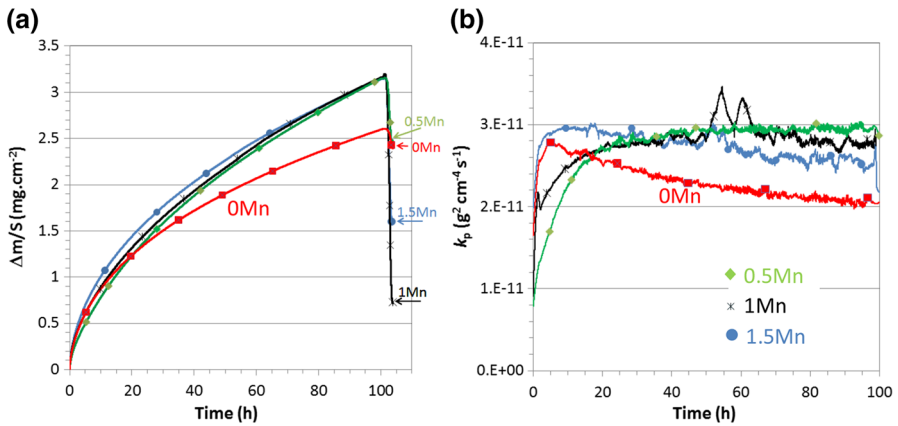
Fig. 2 **a** Oxidation of the studied model alloys during isothermal exposure at 1050 °C in dry air. **b** Time dependence of the instantaneous oxidation rate k_p during isothermal oxidation of Ni–25Cr and Ni–25Cr–xMn ($x = 0.5$, 1, 1.5% wt) (Color figure online)

$$2 \times \frac{\Delta m}{S} \times \frac{d\left(\frac{\Delta m}{S}\right)}{dt} = k_p \qquad (2)$$

At short exposure time (0–20 h), the mass gain (Fig. 2a) is higher for Ni–25Cr than for Ni–25Cr–0.5Mn and Ni–25Cr–1Mn. The instantaneous parabolic constants (Fig. 2b) of Ni–25Cr and Ni–25Cr–1.5Mn decrease with time, while those of Ni–

25Cr–0.5Mn and Ni–25Cr–1Mn increase and stabilize approximately 3×10^{-11} g^2 cm^{-4} s^{-1}. Thus, the addition of 0.5–1 wt% Mn reduces the oxidation rate at short exposure time, but increases the k_p values for $t > 20$ h of exposure at 1050 °C.

The data were also used to determine the parabolic constant using the complete parabolic law [19]. The k_p values determined by this method (Table 2) are close to the instantaneous parabolic constant values presented in Fig. 2b and show that the oxidation rates of Mn-containing alloys are greater by a factor ∼ 1.5 compared to the oxidation rate of the binary Ni–25Cr.
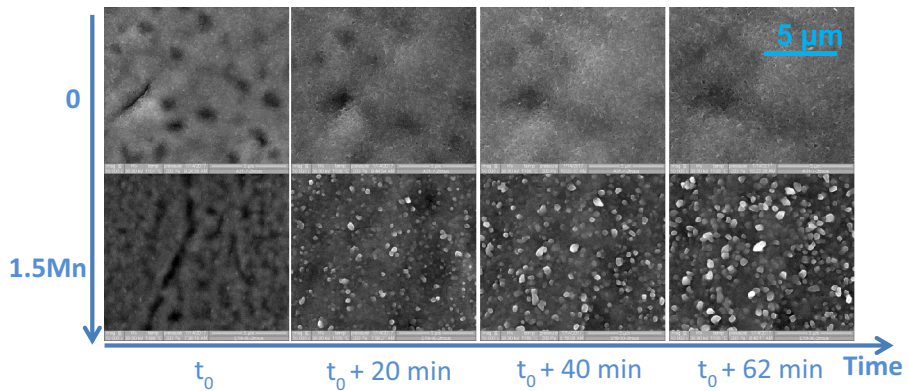
In Situ ESEM Characterizations

The study of the early stages of oxidation has been performed using in situ ESEM. Figure 3 displays the evolution of the surface morphology in the early stages of the oxidation phenomenon for Ni–25Cr and Ni–25Cr–1.5Mn. It is obvious that the oxide surface morphologies are different. Chromia scale formed on Ni–25Cr has an entangled structure, whereas for the Mn-containing sample, crystallite-like morphology grows from the very beginning of oxidation. Initially, dark grey areas develop. This is attributed to heterogeneity in the oxide thickness; the areas with the thinner oxide scale being the dark areas on the pictures. With time, this inhomogeneity tends to disappear in both alloys. With oxidation time, the surface morphology of Ni–25Cr does not change, whereas the crystallite size for Ni–25Cr–xMn alloys increases with time. Post-oxidation observations show that these crystallites correspond to the Mn-containing spinel. The growth rate of these crystallites has been determined redrawing the edges of the grains for 10–15 representative pictures. Figure 4 presents the plots of crystallites' mean radius versus both time and Mn content. An increase in the manganese content to Ni–25Cr alloys results in the increase in the size of spinel crystallites that develop on top of these alloys. It should be noted that the ESEM images are obtained from an area away from the grain boundaries.

The surface morphology of the oxide formed on model alloys after 1 h of oxidation at 1050 °C is shown in Fig. 5. At low magnification, all alloys show swelling lines that are consistent with metal grain boundaries (GB). As commonly acknowledged [20], this suggests that manganese and chromium flows are higher at the alloy grain boundaries than through the lattice of the alloy grains. Thus, the size of the spinel crystallites appears to be slightly larger at the top of a metal grain boundary.

Table 2 Parabolic rate constants calculated for the three model alloys using the complete parabolic law	Alloys (wt%)	k_p (g^2 cm^{-4} s^{-1}) x 10^{11}
	Ni–25Cr	1.9
	Ni–25Cr–0.5Mn	3.35
	Ni–25Cr–1Mn	3.2
	Ni–25Cr–1.5Mn	2.5

Fig. 3 In situ surface characterization by ESEM during oxide growth at 1050 °C in 200 Pa of oxygen for Ni–25Cr and Ni–25Cr–1.5Mn. It is important to note that the same zone of the sample was observed continuously
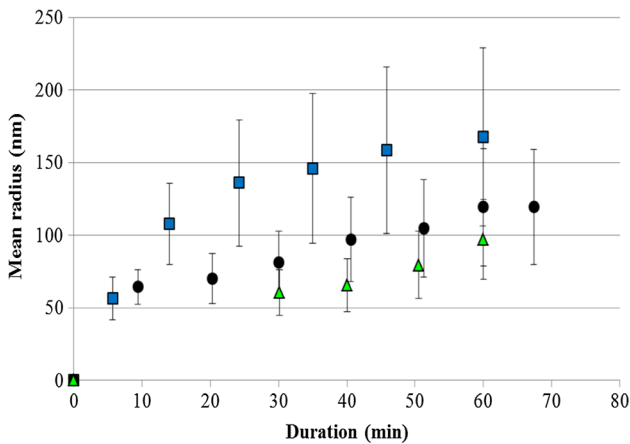

Fig. 4 Oxidation time dependence of crystallites' size for the studied alloys (green triangles = 0.5Mn; black circle = 1Mn; blue square = 1.5Mn) (Color figure online)

Cross-sectional Characterization of ESEM Samples

Figure 6 shows the STEM cross section with Mn and Cr EDX maps of Ni–25Cr–1.5Mn after 1 h of oxidation under 200 Pa of oxygen, with the Mn-rich spinel located on top of the chromia scale as already mentioned above. This scale is continuous after 1 h of oxidation and the thickness of spinel oxide is approximately 250 nm. The pores are located at the chromia-spinel interface. The very low amount of manganese in the chromia scale does not permit its quantification.
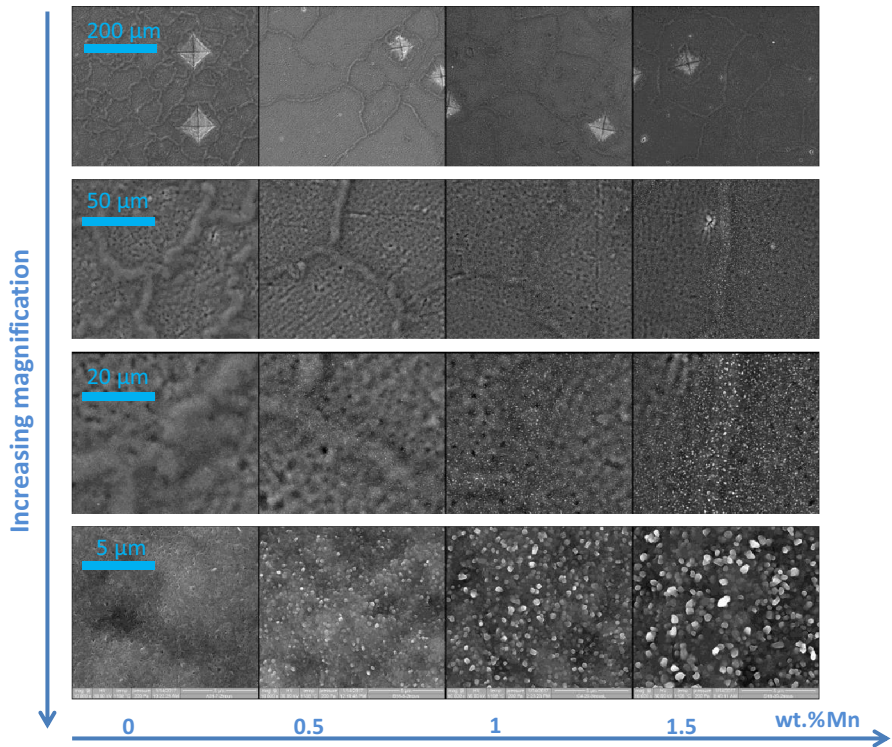
Fig. 5 Comparison of surface states after 1 h oxidation at 1050 °C in 200 Pa of oxygen for Ni–25Cr and Ni–25Cr–xMn. The indents that can be observed in the images at low magnification were performed in order to locate the same areas during the investigation
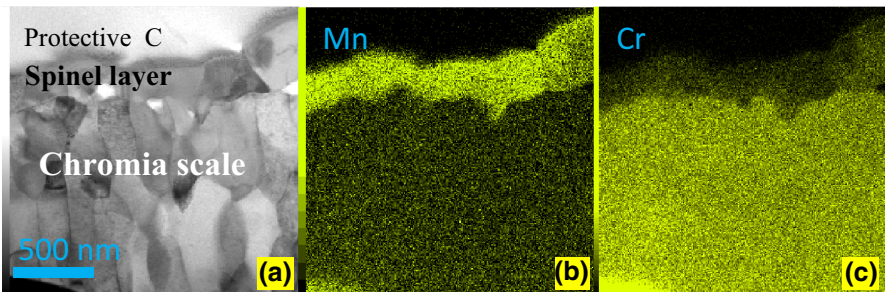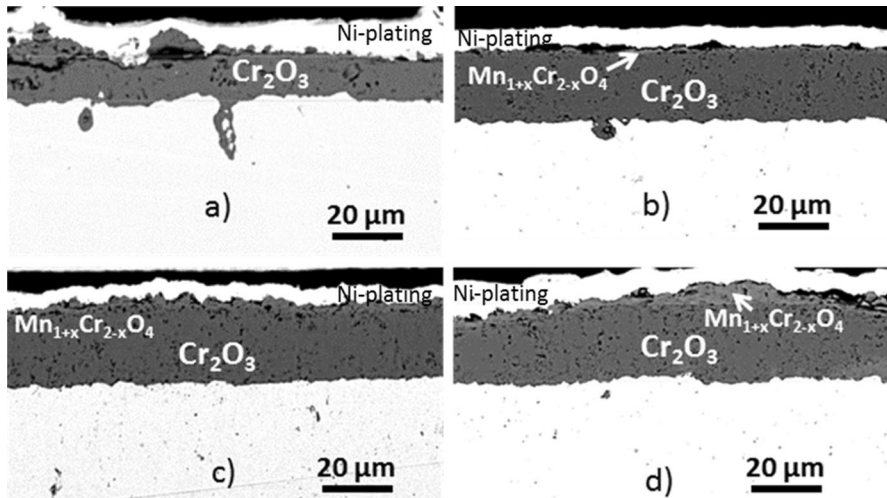

Fig. 6 STEM a, Mn b and Cr c EDX maps for Ni–25Cr–1.5Mn after 1 h of oxidation in 200 Pa of oxygen

Diffusion Profiles

To assess diffusion profiles, the studied model alloys were oxidized for 20 min and for 100 h in ambient air. The cross sections of the alloys after 100 h of oxidation are presented in Fig. 7. The overall oxide thicknesses are quite similar for the Mn-

Fig. 7 SEM cross sections of Ni–25Cr–xMn after 100 h of oxidation under air. **a** Ni–25Cr; **b** Ni–25Cr–0.5Mn; **c** Ni–25Cr–1Mn; **d** Ni–25Cr–1.5Mn

containing samples (20 ± 4 μm) and are higher than for Ni–25Cr (11 ± 3 μm), confirming the higher oxidation rate in the presence of Mn. The continuous layer of manganese-containing spinel is observed regardless of the initial Mn content at the top of the chromia layer. Small pores are located at the chromia-spinel interface. XRD (not shown here) was also performed on the surface of the Ni–25Cr–0.5Mn specimen after 100 h oxidation in air at 1050 °C. The obtained pattern confirms the presence of Cr_2O_3 and the $Mn_{1+x}Cr_{2-x}O_4$ spinel phase.

Microprobe analyses were performed on Ni–25Cr and Ni–25Cr–xMn in order to determine the chromium and manganese diffusion profiles in the alloy after oxidation. The diffusion profiles were evaluated in the alloys in the regions far away from the alloy grain boundaries perpendicular to the surface and starting from the metal–oxide interface.

At short oxidation time (Fig. 8a), the chromium depletion profiles of the four model alloys are in good agreement with the thermogravimetric results (Fig. 2). Indeed, the smallest Cr depletion is observed for the Ni–25Cr–0.5Mn and Ni–25Cr–1Mn alloys which exhibit the smallest mass gain at short time. This is also observed for Ni–25Cr which exhibits a high oxidation rate at short time and then a high Cr depletion. The behaviour of Ni–25Cr–1.5Mn for short-time oxidation is less in agreement with instantaneous k_p data.

At long time (Fig. 8b), the depletion profiles remain in agreement with the thermogravimetric results (Fig. 2). The Ni–25Cr shows the smallest mass gain in comparison with Ni–25Cr–xMn and also exhibits the lowest Cr depletion.

Figure 8c, d shows the Mn diffusion profiles. At short time, Mn depletion extends over 10–15 μm, i.e., the same order of magnitude as the Cr depletion. For long-time oxidation, Mn depletion extents over 150 μm, whereas the chromium concentration profile reaches the initial Cr concentration at approximately 100 μm.
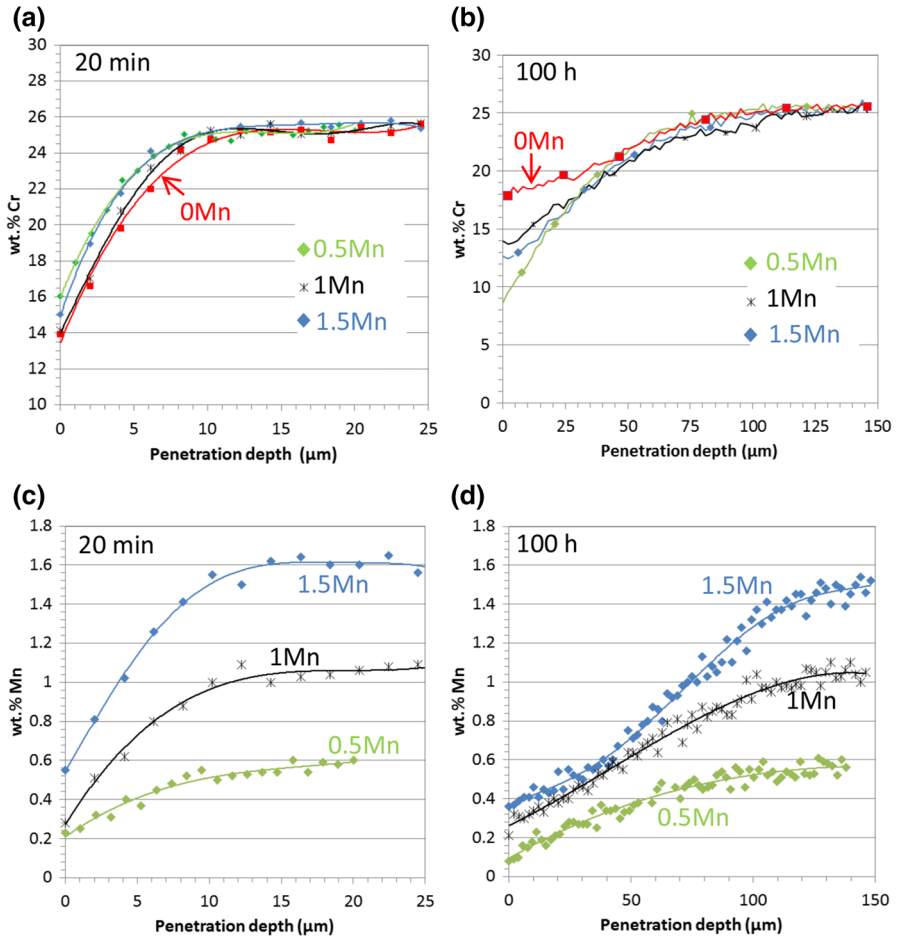
Fig. 8 Depletion profiles of the studied model alloys: **a** Cr depletion profiles after 20 min, **b** Cr depletion profiles after 100 h; **c** Mn depletion profiles after 20 min, **d** Mn depletion profiles after 100 h (Color figure online)

To compare chromium and manganese flows during oxidation, chromium and manganese losses have been estimated from the diffusion profiles of Fig. 8, assuming the metal–oxide interface to be fixed. The obtained results are given in

Table 3 Manganese and chromium mass loss (mg cm^{-2}) at short and long oxidation times

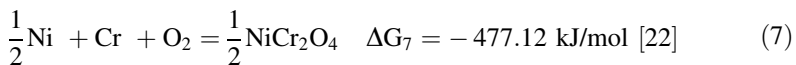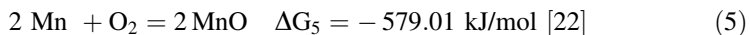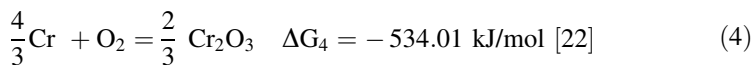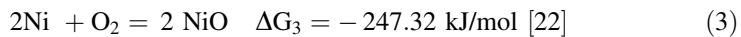| Sample	20 min		100 h	
	Cr	Mn	Cr	Mn
Ni–25Cr	0.5		3.34	
Ni–25Cr–0.5Mn	0.25	0.02	4.07	0.2
Ni–25Cr–1Mn	0.41	0.04	4.85	0.45
Ni–25Cr–1.5Mn	0.32	0.06	4.91	0.90

Table 3. Manganese loss is one order of magnitude lower than chromium loss (approximately 10% of Cr loss), and the loss is somewhat proportional to the initial Mn content for all alloys with the exception of Ni–25Cr–1.5Mn at long time for which the Mn depletion is higher. As a consequence, accounting for the chemical concentration gradient it can be approximated that the manganese interdiffusion coefficient should be at least ten times greater than that of chromium. Literature-reported values [21] are available for the impurity lattice diffusion of manganese in Fe- and Fe–Ni-base alloys at low temperature, but to the best of our knowledge, analogous data are not available for Ni-base alloys. Further investigations are ongoing in order to accurately evaluate these diffusion coefficients.

Discussion

Oxidation of manganese-containing alloys in this study resulted in duplex scales morphology formed during reaction in air. A chromia layer grows at the metal–oxide interface, whereas a continuous layer of $Mn_{1+x}Cr_{2-x}O_4$ spinel was established at the top of the chromia layer.

Thermodynamic Stability of Oxides

Thermodynamic considerations can be taken into account assuming $a_{Mn} = 0.7 \times 10^{-3}$ and $a_{Cr} = 0.39$ [evaluated from TTNi8 ThermoCalc database, for Ni–25Cr–1Mn (in wt%)] and the following oxidation reactions (free Gibbs energy given at 1050 °C):

$$2Ni + O_2 = 2\,NiO \quad \Delta G_3 = -247.32 \text{ kJ/mol [22]} \tag{3}$$

$$\frac{4}{3}Cr + O_2 = \frac{2}{3}\,Cr_2O_3 \quad \Delta G_4 = -534.01 \text{ kJ/mol [22]} \tag{4}$$

$$2\,Mn + O_2 = 2\,MnO \quad \Delta G_5 = -579.01 \text{ kJ/mol [22]} \tag{5}$$

$$\frac{1}{2}Mn + Cr + O_2 = \frac{1}{2}MnCr_2O_4 \quad \Delta G_6 = -581.12 \text{ kJ/mol [22]} \tag{6}$$

$$\frac{1}{2}Ni + Cr + O_2 = \frac{1}{2}NiCr_2O_4 \quad \Delta G_7 = -477.12 \text{ kJ/mol [22]} \tag{7}$$

$$2\,Mn + 2\,Cr_2O_3 + O_2 = 2\,MnCr_2O_4 \quad \Delta G_8 = -740.82 \text{ kJ/mol [22]} \tag{8}$$
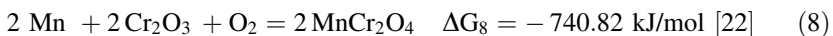
Using these data, it can easily be calculated that all of these oxides are expected to form at 1050 °C in air. However, only Mn- and Cr-containing oxides (Cr_2O_3, $Mn_{1+x}Cr_{2-x}O_4$) are of interest here since only these oxides have been identified by TEM in the present study. Thus, even at short oxidation time, the oxygen partial pressure at the alloy surface is considerably lower or the nucleation and growth of nickel-containing oxides is too sluggish for the formation of the oxides, compared to

chromium and manganese oxides. Considering reactions (4), (5) and (6), the lowest oxygen partial pressure at equilibrium can be calculated from reaction (6), giving the value of 1.1×10^{-21} atm at 1050 °C. Thus, the expected oxide at the metal–oxide interface is $MnCr_2O_4$.

Formation of $Mn_{1+x}Cr_{2-x}O_4$ and Cr_2O_3

The in situ observations have confirmed that the development of spinel occurs at the very beginning of the oxidation. It was possible to distinguish chromia from spinel oxide because these oxides do not develop according to the same morphology in ESEM conditions. Small size crystallites were clearly identified from the moment the samples reach the isothermal dwell, whereas chromia shows an entangled morphology in these conditions. The ESEM observations show that the crystallites are not coalescing at this temperature.

The oxidation kinetics of Mn-containing alloys in air at 1050 °C followed by thermogravimetry results also suggested that the transient period (short-term oxidation) is altered by the addition of Mn. At short term, the oxidation rate is lower for alloys containing low amount of added Mn (0.5 and 1Mn) than for the Ni–25Cr alloy. Figure 2b, showing the instantaneous k_p values vs time, provides evidence that for these Mn-containing alloys, the steady-state regime is reached only after 20 h of oxidation at 1050 °C, whereas this is not the case for Ni–25Cr even after 100 h. Thus, it can be proposed that the lowest oxidation rate observed at short-term exposure for Mn-containing alloys may result from the competition that exists between manganese and/or chromium oxides formation.

The fact that Mn-containing spinel is not observed at the metal–oxide interface on post-oxidation cross sections should be due to the rapid manganese consumption at the metal–oxide interface in the short term, as proposed previously [1]. The concentration profiles presented in Fig. 8, which are the results of complementary oxidation tests carried out in a tubular furnace in laboratory air, confirm this suggestion. Longer diffusion distances have been observed for Mn than for Cr for all samples, suggesting a higher diffusion rate for manganese than for chromium in the austenitic Ni–Cr lattice.

Then, the Mn rapid consumption may reduce the manganese activity below $a_{Mn} = 1 \times 10^{-4}$, corresponding to the value at which the development of chromia scale is thermodynamically expected for the alloy Ni–25Cr–1Mn (in wt%).

The oxidation kinetics of Mn-containing alloys in air at 1050 °C also suggested that manganese can have a significant effect on the scale growth rate at long time, increasing the k_p values by a factor as high as 1.5 relative to the k_p value of a manganese-free Ni–25Cr obtained using the same manufacturing routes. This effect was already noticed by Zurek et al. [9] in their work comparing the oxidation rates of Ni–25Cr and Ni–25Cr–0.5Mn in Ar-20% O_2. The increase in k_p values could be attributed to an acceleration of the chromia growth rate. This phenomenon may be explained by Mn^{2+} doping the chromia scale according to Eq. (9) [23], showing that the substitution of Cr by Mn induces an increase in the amount of oxygen vacancies which are believed to be the main defect at low-oxygen partial pressure [24].

$$2 \text{ MnO} = 2 \text{ Mn}'_{Cr} + 2 \text{ O}_O + \text{ V}_O^{\cdot\cdot} \tag{9}$$

Moreover, Mn additions lead to severe spallation of the oxide scale on cooling in comparison with the Mn-free alloy (Fig. 2a) showing the effect of the manganese spinel on the mechanical behaviour of the oxide scale; this point should be studied further.

Discussion of In Situ Examinations

In situ oxidation in SEM has been a powerful tool for the examination of the early stage of oxidation in the present study. However, the interpretation of its results should be carefully done because the specific conditions of use can themselves have a significant effect on the oxidation process. For example, Fig. 9 compares the surface morphology of both Ni–25Cr and Ni–25Cr–xMn alloys for in situ oxidation in ESEM in low-oxygen pressure (200 Pa) and 1 h oxidation in dry air used in these experiments. The oxygen pressure does not modify the surface morphology of the Mn-containing alloys that form spinel at the top of the oxide layer, but strongly impacts the external morphology of the chromia forming on Ni–25Cr alloy. Simon et al. [25] previously reported that large chromia crystallites develop in air, whereas the ones formed in Ar-7%H$_2$O appear entangled. Latu-Romain et al. [24] reported the same structure in low P$_{O2}$ (10^{-12} atm). In addition to this obvious effect, there may be other effects of the oxygen partial pressure on chromia grains growth that have not been yet evidenced in our investigation. Therefore, the in situ oxidation
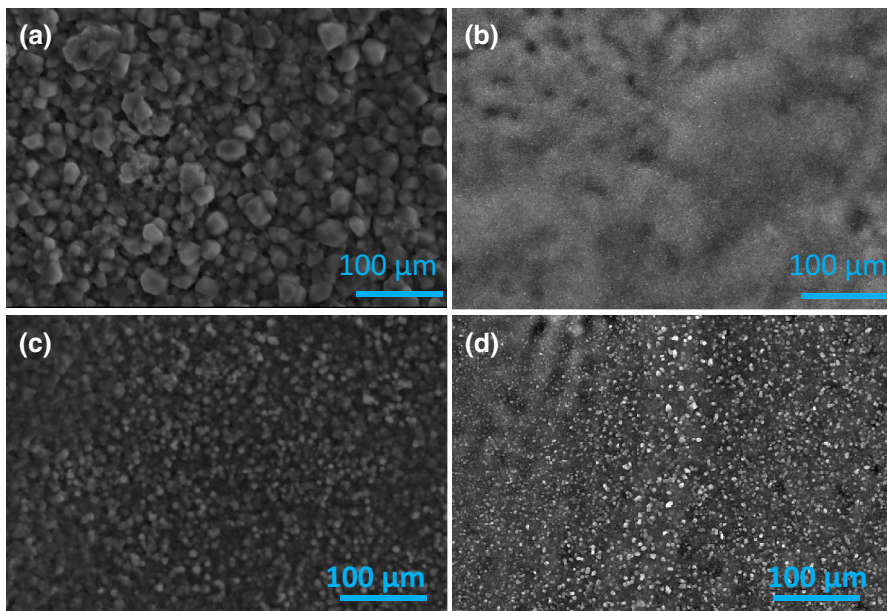
Fig. 9 Surface morphologies of samples oxidized 1 h at 1050 °C: Ni–25Cr **a** in air and **b** in ESEM with 200 Pa O$_2$ and Ni–25Cr–1.5Mn **c** in air and **d** in ESEM with 200 Pa O$_2$

results cannot be fully extrapolated to the oxidation mechanism in air. Further experiments are now required to determine whether this change of morphology has an impact on the oxidation kinetics.

Conclusions

The oxidation rates of Mn-containing Ni–25Cr model alloys were determined in air using thermogravimetric tests. Mn addition increases the oxidation kinetics by the factor of 1.5 at long time, whereas at short time, the Ni–25Cr–0.5Mn and Ni–25Cr–1Mn alloys exhibit smaller parabolic rates than Ni–25Cr. This has been attributed to the competition between the formation of chromia and spinel, the latter being the thermodynamically expected oxide at the metal interface for a Ni–25Cr–1Mn alloy. ESEM shows that the spinel crystallites form from the very beginning of the oxidation. This spinel layer develops and is continuous on top of the chromia scale regardless of the manganese concentration. Manganese and chromium diffusion profiles measurements show that Mn has a higher diffusion coefficient than Cr in the studied alloys. Mn is rapidly consumed at the beginning of the exposure at high temperature, allowing the formation of chromia at the metal–oxide interface.

ESEM observations carried out with 200 Pa oxygen reveals that surface morphology of the Ni–25Cr alloy differs from that obtained after oxidation is carried out in air. Thus, the ESEM results cannot be directly used to extrapolate the oxidation mechanism of these alloys in air. Further studies will be devoted to the assessment of impurity lattice diffusion coefficient of Mn and to the quantification of the Mn effect on oxidation with water vapour.

References

1. D. J. Young, *High Temperature Oxidation and Corrosion of Metals*, (Elsevier, Oxford, 2008).
2. J. H. Chen, P. M. Rogers, and J. A. Little, *Oxidation of Metals* **47**, 381 (1997).
3. X. Ledoux, S. Mathieu, M. Vilasi, Y. Wouters, P. Del-Gallo, and M. Wagner, *Oxidation of Metals* **80**, 25 (2013).
4. S. C. Tsai, A. M. Huntz, and C. Dolin, *Materials Science and Engineering A* **212**, 6 (1996).
5. R. Prescott and M. J. Graham, *Oxidation of Metals* **38**, 233 (1992).
6. B. A. Pint, *Oxidation of Metals* **45**, 1 (1996).
7. P. J. Smith, O. Biest, and J. Corish, *Oxidation of Metals* **24**, 277 (1985).
8. V. Badin, E. Diamanti, P. Forêt, and E. Darque-Ceretti, *Oxidation of Metals* **82**, 347 (2014).
9. J. Zurek, D. J. Young, E. Essuman, M. Hänsel, H. J. Penkalla, L. Niewolak, and W. J. Quaddakers, *Materials Science and Engineering A* **477**, 259 (2008).
10. F. H. Stott, F. I. Wei, and C. A. Enahoro, *Materials and Corrosion* **40**, 198 (1989).
11. D. L. Douglass and J. S. Armijo, *Oxidation of Metals* **2**, 207 (1969).
12. S. N. Basu and G. J. Yurek, *Oxidation of Metals* **36**, 281 (1991).
13. D. Oquab, N. Xu, D. Monceau, and D. J. Young, *Corrosion Science* **52**, 255 (2010).
14. D. Kim, C. Jang, and W. S. Ryu, *Oxidation of Metals* **71**, 271 (2009).
15. G. R. Holcomb and D. E. Alman, *Scripta Materialia* **54**, 1821 (2006).

16. E. J. Opila, D. L. Myers, N. S. Jacobson, I. M. B. Nielsen, D. F. Johnson, J. K. Olminsky, and M. D. Allendorf, *The Journal of Physical Chemistry A* **111**, 1971 (2007).
17. R. Podor, D. Pailhon, J. Ravaux, and H.-P. Brau, *Microscopy and Microanalysis* **21**, 307 (2015).
18. C. A. Schneider, W. S. Rasband, and K. W. Eliceiri, *Nature Methods* **9**, 671 (2012).
19. D. Monceau and B. Pieraggi, *Oxidation of Metals* **50**, 477 (1998).
20. H. Mehrer, *Diffusion in Solids: Fundamentals, Methods, Materials, Diffusion-Controlled Processes*, (Springer, Berlin, 2007).
21. T. D. Nguyen, J. Zang, and D. J. Young, *Corrosion Science* **112**, 110 (2016).
22. I. Barin and G. Platzki, *Thermochemical Data of Pure Substances*, (VCH, Weinheim, NY, 1995).
23. P. Kofstad, *Nonstoichiometry, Diffusion, and Electrical Conductivity in Binary Metal Oxides*, (Wiley-Interscience, New York, 1972).
24. L. Latu-Romain, Y. Parsa, S. Mathieu, M. Vilasi, M. Ollivier, A. Galerie, and Y. Wouters, *Oxidation of Metals* **86**, 497 (2016).
25. B. Simon, M. Gorr, V. Hänsel, V. Shemet, H.-J. Christ, and W. J. Quadakkers, *Materials at High Temperatures* **32**, 238 (2015).